

## Adaptive optics for confocal laser scanning microscopy with adjustable pinhole

Yoo, H.W.; van Royen, M.E.; van Cappellen, WA; Houtsmuller, AB; Verhaegen, Michel; Schitter, G

**DOI**

[10.1117/12.2227775](https://doi.org/10.1117/12.2227775)

**Publication date**

2016

**Document Version**

Final published version

**Published in**

Proceedings of SPIE

**Citation (APA)**

Yoo, H. W., van Royen, M. E., van Cappellen, WA., Houtsmuller, AB., Verhaegen, M., & Schitter, G. (2016). Adaptive optics for confocal laser scanning microscopy with adjustable pinhole. In J. Popp, V. V. Tuchin, D. L. Matthews, & F. S. Pavone (Eds.), *Proceedings of SPIE: Biophotonics: Photonic Solutions for Better Health Care V* (Vol. 9887). Article 988739 (Proceedings of SPIE; Vol. 9887). SPIE. <https://doi.org/10.1117/12.2227775>

**Important note**

To cite this publication, please use the final published version (if applicable).  
Please check the document version above.

**Copyright**

Other than for strictly personal use, it is not permitted to download, forward or distribute the text or part of it, without the consent of the author(s) and/or copyright holder(s), unless the work is under an open content license such as Creative Commons.

**Takedown policy**

Please contact us and provide details if you believe this document breaches copyrights.  
We will remove access to the work immediately and investigate your claim.

# Adaptive Optics for Confocal Laser Scanning Microscopy with Adjustable Pinhole

Han Woong Yoo<sup>a,c</sup>, Martin E. van Royen<sup>b</sup>, Wiggert A. van Cappellen<sup>b</sup>,  
Adriaan B. Houtsmuller<sup>b</sup>, Michel Verhaegen<sup>c</sup>, and Georg Schitter<sup>a</sup>

<sup>a</sup>Automation and Control Institute (ACIN), Vienna University of Technology, Gusshausstr.  
27-29, 1040 Vienna, Austria;

<sup>b</sup>Erasmus Optical Imaging Center, Department of Pathology, Josephine Nefkens Institute,  
Erasmus Medical Center, Dr. Molewaterplein 50, 3015 GE, Rotterdam, the Netherlands;

<sup>c</sup>Delft Center for Systems and Control, Delft University of Technology, Mekelweg 2, 2628 CD  
Delft, the Netherlands

## ABSTRACT

The pinhole plays an important role in confocal laser scanning microscopy (CLSM) for adaptive optics (AO) as well as in imaging, where the size of the pinhole denotes a trade-off between out-of-focus rejection and wavefront distortion. This contribution proposes an AO system for a commercial CLSM with an adjustable square pinhole to cope with such a trade-off. The proposed adjustable pinhole enables to calibrate the AO system and to evaluate the imaging performance. Experimental results with fluorescence beads on the coverslip and at a depth of 40  $\mu\text{m}$  in the human hepatocellular carcinoma cell spheroid demonstrate that the proposed AO system can improve the image quality by the proposed calibration method. The proposed pinhole intensity ratio also indicates the image improvement by the AO correction in intensity as well as resolution.

**Keywords:** Adaptive Optics, Square Adjustable Pinhole, Confocal Laser Scanning Microscopy, Pinhole Intensity Ratio

## 1. INTRODUCTION

A pinhole is a key component in confocal laser scanning microscopy (CLSM), providing axial resolution by rejecting out-of-focus light. This sectioning ability allows recording a 3D structure of specimen, making CLSM popular in biological fluorescence imaging.<sup>1</sup> The size of the pinhole directly influences the resolution and the intensity of images:<sup>2,3</sup> a bigger pinhole provides more intensity while the resolution of CLSM becomes worse, and vice versa. For this trade-off, microscope manufacturers provide an adjustable pinhole in their CLSM for users to choose the pinhole size based on their specimen condition and imaging need.<sup>4</sup>

The pinhole plays an important role in adaptive optics (AO) for CLSM as well. For sensorless AO, the size of pinhole influences the final correction quality, and the small enough pinhole is necessary to achieve a high Strehl ratio.<sup>5</sup> For the AO with wavefront sensors, such as Shack Hartmann wavefront sensors (SH-WFS), the pinhole can be also used to reject out-of-focus light.<sup>6</sup> Fig. 1 illustrates a confocal wavefront sensor in CLSM with sparse fluorescence molecules in a 3D gel. Without a pinhole, the fluorescence from the out-of-focus region is imaged on the wavefront sensor with in-focus light, degrading the wavefront sensing performance by extending spot images. With a pinhole, the confocal wavefront sensor rejects the fluorescence from the out-of-focus region and maintains the fluorescence at the focus for wavefront sensing. By this reason most AO developments for CLSM usually have a pinhole in front of the SH-WFS for separating the targeted light source from the other sources around<sup>7</sup> and for suppressing the light from the uninteresting out-of-focus region.<sup>6,8-11</sup> The size of the pinhole should be selected carefully considering the trade-off of the sectioning ability and wavefront distortion.<sup>11,12</sup> For selecting the correct pinhole size, the maximum spatial frequency of the targeted aberrations<sup>6,8</sup> and optical sectioning ability in wavefront sensing<sup>12</sup> are considered, while they all use a fixed size pinhole.

---

Further author information: (Send correspondence to Han Woong Yoo)

Han Woong Yoo: E-mail: yoo@acin.tuwien.ac.at, Telephone: +43 1 58801 376518

Biophotonics: Photonic Solutions for Better Health Care V, edited by Jürgen Popp, Valery V. Tuchin,  
Dennis L. Matthews, Francesco Saverio Pavone, Proc. of SPIE Vol. 9887, 988739  
© 2016 SPIE · CCC code: 0277-786X/16/\$18 · doi: 10.1117/12.2227775

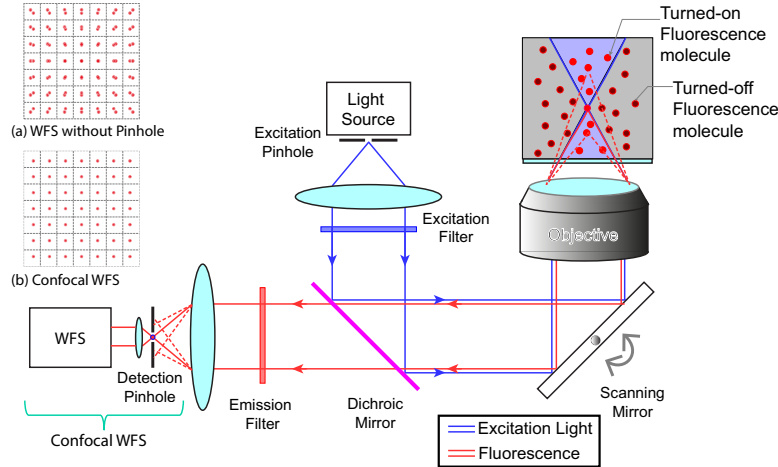


Figure 1. Schematic of a confocal wavefront sensor with CLSM. Molecules of in the light path, shown as blue triangles in the specimen, are excited and generate fluorescence in a volume, which degrades the wavefront sensor spot images. By adding a pinhole in front of the wavefront sensor, fluorescence molecules at the focal region are selected for wavefront sensing and out-of-focus fluorescence is rejected, corresponding to the principle of confocal laser scanning microscopy.

This paper describes an AO development for CLSM with an adjustable square pinhole to compensate for aberrations in the optical system and the specimen. The adjustable pinhole allows flexibility for the trade-off between out-of-focus light rejection and distortion of the aberration. Using the adjustable pinhole, a calibration method for the AO system is proposed to compensate for aberrations in the designed optical system. In addition a pinhole intensity ratio is also proposed to evaluate improvement of the image quality by the AO correction. Experimental results with fluorescence beads on the coverslip and at a depth of 40  $\mu\text{m}$  in a sphere cell cluster show the improved image quality by the proposed AO and the benefits of the proposed calibration method and the quality measure.

## 2. ADAPTIVE OPTICS WITH ADJUSTABLE PINHOLE

### 2.1 AO Calibration via Adjustable Pinhole

The calibration of an AO system with a wavefront sensor is important to decide a target quality by the aberration compensation. That is because flattening a deformable mirror (DM) does not guarantee the flat wavefront at the specimen and the detector due to the aberrations induced by the imaging path, for example, the interface between the microscope and the AO system and the mismatch between the immersion medium and the coverslip. Wavefront sensorless AO system can maximize the image quality without any reference while it need an amount of correction time to record a number of images.<sup>13</sup>

The proposed calibration method exploits an adjustable pinhole to obtain a reference wavefront considering all optical paths from the specimen to the detector. Consider a 4f system<sup>3</sup> by two lenses of focal lengths of  $f_1$  and  $f_2$  with a square pinhole as shown in Fig. 2. Define  $P_{in}(\vec{\xi})$  and  $P_{out}(\vec{\rho})$  as complex functions of input and output pupil, where  $\vec{\rho} = [\rho_x \ \rho_y]^T$  and  $\vec{\xi} = [\xi_x \ \xi_y]^T$  are coordinates of the each pupil plane. The pupil function of the adjustable square pinhole can be written as a square function as

$$P_{ph}(\vec{r}, \vec{\gamma}) = \begin{cases} 1 & |r_x| < \gamma_x/2 \text{ and } |r_y| < \gamma_y/2 \\ 0 & \text{otherwise.} \end{cases} \quad (1)$$

where  $\vec{\gamma} = [\gamma_x \ \gamma_y]^T$  denotes the size of the pinhole and  $\vec{r} = [r_x \ r_y]^T$  is a coordinate at the focal plane. By Fresnel approximation the influence of the pinhole to the output pupil function can be written as follows<sup>3</sup>

$$P_{out}(\vec{\rho}, \vec{\gamma}) = M^{-3} \frac{k^2}{f_1^2} e^{i4\pi k(f_1+f_2)} \mathcal{P}_{ph}\left(\frac{k}{f_2} \vec{\rho}, \vec{\gamma}\right) * P_{in}\left(\frac{1}{M} \vec{\rho}\right), \quad (2)$$

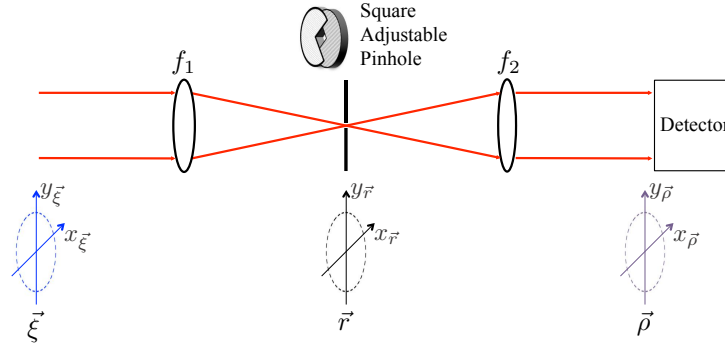


Figure 2. Schematic of the back focal plane and imaged back focal plane through the square adjustable pinhole at the focus.

where  $*$  denotes a 2D convolution operator,  $k$  denotes a wave vector,  $M = -\frac{f_2}{f_1}$  is the magnification between the input pupil and the output pupil.  $\mathcal{P}_{ph}(\vec{\rho}, \gamma_m)$  denotes 2D Fourier transform of the pupil function  $P_{ph}(\vec{r}, \vec{\gamma})$  as

$$\mathcal{P}_{ph}(\vec{\kappa}_{\vec{r}}, \vec{\gamma}) = \iint P_{ph}(\vec{r}, \vec{\gamma}) e^{-i2\pi\vec{r}\cdot\vec{\kappa}_{\vec{r}}} d^2\vec{r}, \quad (3)$$

where  $\vec{\kappa}_{\vec{r}}$  denotes spatial frequency at the focal plane  $\vec{r}$ . Applying Fourier transform to both sides of Eq. (2) and  $\vec{\kappa}_{\vec{\rho}} = -\frac{\kappa}{f_2}\vec{r}$ , the Fourier transform of the output pupil function  $P_{out}$  is given as<sup>3</sup>

$$\mathcal{P}_{out}\left(-\frac{k}{f_2}\vec{r}, \vec{\gamma}\right) = M e^{i4\pi k(f_1+f_2)} P_{ph}(\vec{r}, \vec{\gamma}) \times \mathcal{P}_{in}\left(\frac{k}{f_1}\vec{r}\right) \quad (4)$$

where  $\mathcal{P}_{in}$  denotes the Fourier transform of the input pupil function  $P_{in}$ .

This shows that the spatial frequency of the output pupil function is limited by the pupil function of the pinhole. For instance, an extremely small pinhole, a delta function, only selects the lowest spatial frequency of the pupil function, i.e. a flat wavefront regardless of the input pupil function. This is also shown in Eq. (2) that the input pupil function is convoluted by the Fourier transformed pinhole function. Using this band-limited aberration through the small pinhole, an AO calibration method via adjustable pinhole is proposed as follows.

1. Set a reference grid for SH-WFS with a big pinhole.
2. Measure the wavefront with a small pinhole, and regards it as a new reference of SH-WFS.
3. With a big pinhole, compensate for the aberrations by the DM according to the updated reference in 2.

## 2.2 Image Quality Measure using Adjustable Pinhole

For the evaluation of the image quality by the AO corrections, image intensity, full width at half maximum (FWHM), and image sharpness are traditionally used.<sup>6, 8, 14</sup> These measures use the same specimen to evaluate the improvement by the AO correction. For the fluorescence specimen, however, photobleaching makes the measurement time-dependent: the intensity of the specimen itself drops during the aberration correction and imaging. For a long-time measurement with easily bleached specimen, the evaluation of the improvement by AO therefore cannot be compared by the increase of the sample image intensity. FWHM could be a solution but it depends on the size and the shape of specimen.

To measure the quality of AO correction, a pinhole intensity ratio, a new quality measure of aberration for confocal microscopy, is proposed by using scanned images with two different pinhole sizes as

$$J_r = \frac{\max I_c(x, y, z, \vec{\gamma}_s)}{\max I_c(x, y, z, \vec{\gamma}_b)}, \quad (5)$$

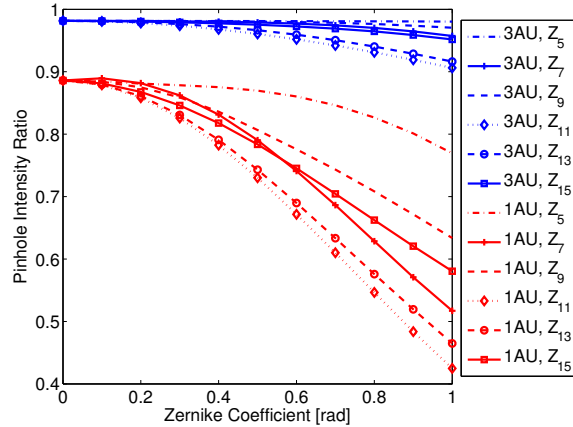


Figure 3. Simulation results of the pinhole intensity ratio by a square adjustable pinhole for the single Zernike aberration. The small pinhole size is set by 3 AU and 1 AU while the size of big small pinhole is set by 5 AU. In the simulation the maximum is chosen in the lateral image at the focus, i.e. 2D imaging is assumed.

where  $I_c(x, y, z, \vec{\gamma})$  are recorded confocal intensity by  $x$ ,  $y$ , and  $z$  scanning with a pinhole  $\vec{\gamma}$ , and  $\vec{\gamma}_s$  and  $\vec{\gamma}_b$  denote a small and a big pinhole, respectively. Assuming that the source is point-like, then the pinhole intensity ratio can be rewritten by Parseval's theorem and Eq. (4) as<sup>15</sup>

$$J_r = \frac{\iint_{S_{\vec{\gamma}_s}} \left| \mathcal{P}_{in} \left( \frac{\kappa}{f_1} \vec{r} \right) \right|^2 d^2 \vec{r}}{\iint_{S_{\vec{\gamma}_b}} \left| \mathcal{P}_{in} \left( \frac{\kappa}{f_1} \vec{r} \right) \right|^2 d^2 \vec{r}}, \quad (6)$$

where  $S_{\vec{\gamma}}$  is an area defined by  $\vec{\gamma}$  as Eq. (1). This pinhole intensity ratio provides the ratio of the power of low frequencies in the input pupil compared to the total power of a wide frequency range. The benefit of this measure is that the amount of aberrations can be promptly evaluated by an additional image with manipulating the adjustable pinhole, which can provide a normalized measure in a different specimen and different detection gain. Tip and tilt aberrations do not influence this measure because it is compensated by 2D scanning and defocus does not influence the measure with 3D imaging as well.

Fig. 3 shows a simulation result of the pinhole intensity ratio for each Zernike mode by setting 5 AU as a big pinhole and 3 AU and 1 AU pinhole as a small pinhole. Similar to Strehl ratio, this pinhole intensity ratio decreases as aberrations increase since the low frequency component of the Fourier domain is dominant with low aberrations. The decrement of pinhole intensity ratio is not vivid with 3 AU of pinhole while it is with 1 AU of pinhole.

### 3. EXPERIMENTAL SETUP

#### 3.1 Adjustable Square Pinhole

For the experimental setup, a square adjustable pinhole (20-600  $\mu\text{m}$ , TCS MR2, a part of Leica SP2 confocal microscope, Leica Microsystems, Mannheim, Germany) is used to reject out-of-focus light for CLSM imaging and wavefront sensing.<sup>4</sup> The adjustable pinhole module operates with a stepper motor controlled by Matlab (The MathWorks, Inc., Natick, Massachusetts, USA) via a stepper driver (Stellaris Stepper Motor Reference Design Kit, Texas Instruments, Dallas, TX, USA). The size of the pinhole is calibrated by a digital microscope (VHX-100, Keyence, Osaka, Japan) in advance.

#### 3.2 Optical System Design

Fig. 4 shows an experimental setup of the AO system for Leica SP5 confocal microscope. The light source for excitation path is a HeNe laser (633 nm, 7 mW, 1125P, JDSU) with a polarizer for the intensity adjustment. L1 ( $f=11$  mm, A397TM-A, Thorlabs, Newton, NJ, USA) and L2 ( $f=60$  mm, AC254-060-A-ML, Thorlabs) with

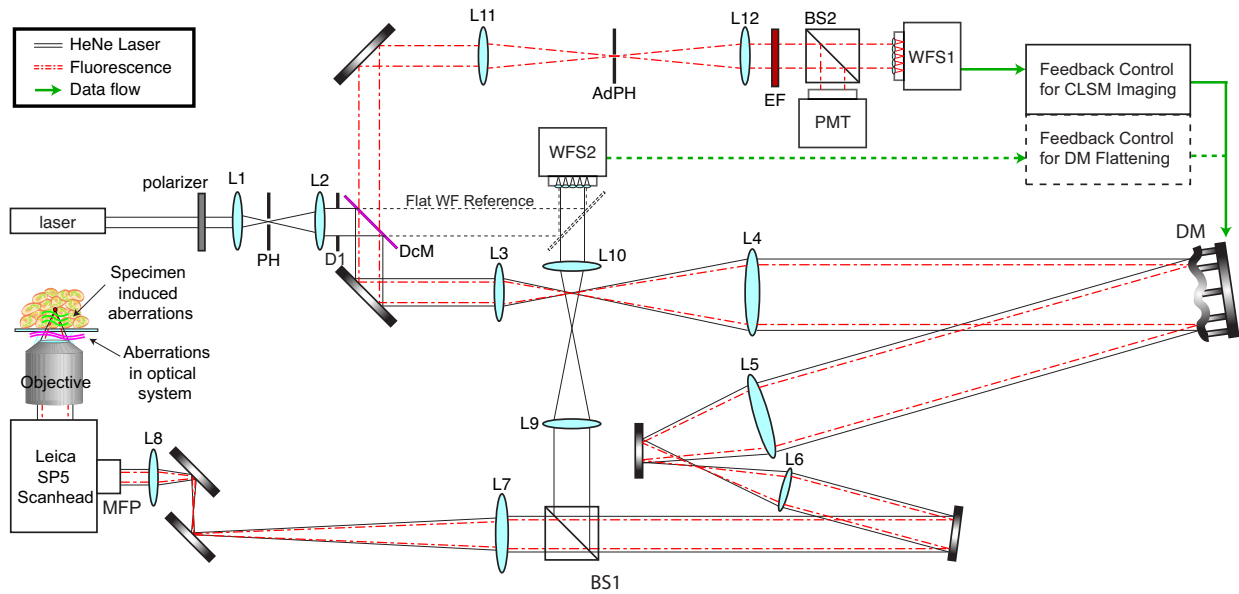


Figure 4. Schematic of the AO experimental setup for a Leica SP5 confocal microscope via a multifunctional port (MFP). Black solid lines represent the path of HeNe laser (633 nm) and red dash-dot lines represent the path of fluorescence. The laser is spatially filtered through the excitation pinhole (PH) and expanded to illuminate a piezoelectric deformable mirror (DM), which is conjugated with the back focal plane of the microscope objective. Then the beam is contracted for entering the MFP of the Leica SP5 scanhead while a part of the beam is sampled for monitoring the DM shape by a wavefront sensor (WFS2) and initial DM flattening by a feedback control (dotted green line with a dotted black box). The laser beam focused on the specimen generates fluorescence while both light paths suffer from the aberrations induced by the imperfect optical system (magenta wavy lines) and the specimen (green wavy lines). The fluorescence is collected by the same path through the MFP and the DM until a dichroic mirror (DcM). The DcM branches the detection path for fluorescence and the fluorescence passes through an adjustable pinhole (AdPH) and an emission filter (EP) and is gathered by a photomultiplier tube (PMT, Leica RLD) and a wavefront sensor for fluorescence (WFS1). This WFS1 is used for the AO compensation (green solid line with a black box).

a fixed pinhole (10  $\mu\text{m}$ , Thorlabs) generate a clear Gaussian pupil at the aperture D1. This beam is expanded to 23 mm for a 19 channel piezoelectric actuated deformable mirror DM (30 mm 19 channel, Flexible Optical B.V.) by L3 ( $f=200\text{ mm}$ , AC254-200-A-ML, Thorlabs) and L4 ( $f=750\text{ mm}$ , AC508-750-A-ML, Thorlabs). After a wavefront modification by the DM, the beam is contracted by L5 ( $f=500\text{ mm}$ , AC508-500-A-ML, Thorlabs) and L6 ( $f=150\text{ mm}$ , AC254-150-A-ML, Thorlabs). Then the beam is split into two by a non-polarization cube beam splitter BS1 (90% transmission and 10% reflection, BS025, Thorlabs), and the sampled beam is used for the wavefront measurement by Shack Hartmann wavefront sensor WFS2 (200  $\mu\text{m}$  pitch  $f = 10\text{ mm}$  orthogonal grid lenslet array, APO-Q-P192-F3.17, UEye UI-2210SE CCD camera, Flexible Optical B.V., Rijswijk, the Netherlands), which is conjugated with DM by L9 ( $f=300\text{ mm}$ , AC254-300-A-ML, Thorlabs) and L10 ( $f=150\text{ mm}$ , AC254-150-A-ML, Thorlabs). The transmitted beam is contracted by L7 ( $f=750\text{ mm}$ , AC508-750-A-ML, Thorlabs) and L8 ( $f=300\text{ mm}$ , AC254-300-A-ML, Thorlabs) and used for the excitation of the fluorescence in the specimen through Leica multi functional port (MFP). Through MFP, the DM is conjugated with the back focal plane of the objective (1.25 NA oil immersion, HCX PL APO 40 $\times$ , 506179, Leica Microsystems).

The emission of fluorescence from specimen follows the same path until a dichroic mirror DcM (651 nm cut on/off, zt638rdc, Chroma Technology, Bellows Falls, VT, USA). After the dichroic mirror the fluorescence passes through L11 ( $f=500\text{ mm}$ , AC254-500-A-ML, Thorlabs) and the adjustable square pinhole. The beam after the adjustable pinhole is collimated by L12 ( $f=400\text{ mm}$ , AC254-400-A-ML, Thorlabs) and passes through an emission filter (650 nm cut on/off, ET650LP, Chroma Technology) and separated into two by a non-polarization cube beam splitter BS2 (50% transmission and 50% reflection, BS013, Thorlabs). These two separated beams are collected by a photomultiplier tube PMT (RLD type non-descanned detector, a custom made, Leica Microsystems) and a Shack Hartmann wavefront sensor WFS1 (Coolsnap HQ2 CCD Camera, Photometrics, Tucson, AZ, USA, with

a lenslet array of  $300\ \mu\text{m}$  pitch  $f = 18\ \text{mm}$  orthogonal grid, Flexible Optical B.V). The WFS1 is also conjugated with the DM as WFS2.

There are modifications of Leica SP5 for the AO system. An infrared mirror in the MFP is replaced with a broadband dielectric mirror for the visual spectrum (400-850nm, BB05-E02, Thorlabs) to connect both excitation and emission path to the AO system. The RLD is also an order-made for fluorescence detection over 650nm. With this modification, the entire CLSM with the AO system is still intact with the Leica scanhead and can be directly operated by the software of the Leica, which is convenient to record and process CLSM images.

The entire optical system including the interface between the AO and Leica SP5 is aligned with the flattened DM by maximizing axial intensity of a flat mirror slide at the specimen. This flattened DM is regarded as an uncompensated system in the experiments since it provides the best intensity by given alignment of the optical system.

For the wavefront sensing from fluorescence by WFS1, the exposure time is set by 2 s to collect the enough intensity. With this long exposure time, a single fluorescence bead with a focused beam is usually bleached during the wavefront sensing. To reduce photobleaching, the beam scans fluorescence beads in a given area,  $21.64 \times 20.94\ \mu\text{m}^2$ , while the WFS1 is accumulating the light, allowing extended correction and measurement time. This scanning motion during wavefront sensing extends the lifetime of fluorescence beads.

### 3.3 Control System Design

In the AO system the DM is regulated by the measured wavefront of fluorescence by WFS1 through the specimen and the optical system. The control system of the developed AO system follows the control system in Ref. 16 with minor differences in geometry matrix and influence matrix calculation. For the calculation of the geometry matrix of the wavefront sensor, a Zernike based reconstruction is used.<sup>17</sup> The influence matrix is calculated by the inputs to the DM and the wavefront measurements from the beads on the coverslip. To obtain high linearity of the piezoelectric DM, every input is applied shortly after a degauss function,<sup>18</sup> which is a linearly attenuated sinusoidal signal to prevent abrupt changes of the piezoelectric actuators. For the numerically stable inversion in the influence matrix calculation, truncated SVD is used.<sup>19</sup> For all measurements, tip, tilt and defocus are ignored to remove the specimen-dependency because they are regarded as a displacement error.<sup>20,21</sup>

### 3.4 Specimen Preparation

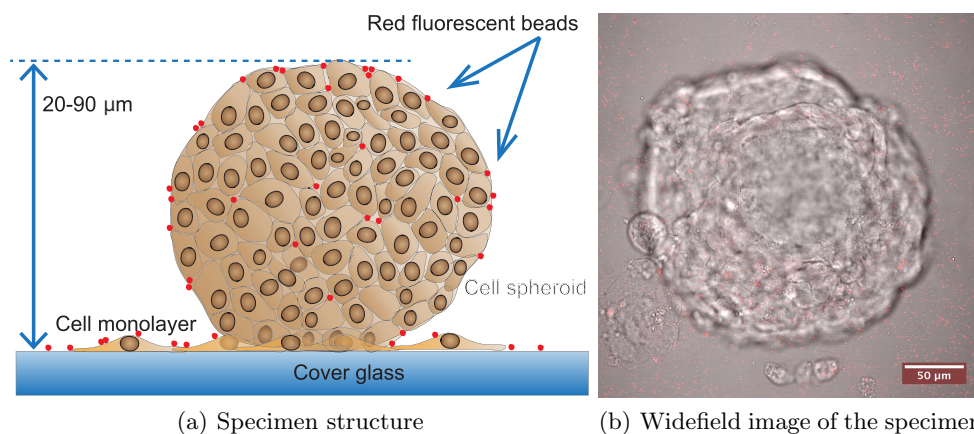


Figure 5. Specimen for the evaluation of the developed AO system. (left) an illustration of a cellular spheroid of human hepatocellular carcinoma (Hep3B) cells with fluorescence beads sprinkled on the coverslip and in the spheroid. (Right) A wide field image (grayscale) of the cellular spheroid with an overlaid confocal image of fluorescence beads (red dots). The focus is at the interface of specimen and coverslip.

To simulate aberrations in a tissue-like environment, a 3D cell culture system shown in Fig. 5(a) is used. Human hepatocellular carcinoma (Hep3B) cells are grown in  $25\text{cm}^2$  cell culture flasks with an ultra-low attachment surface to allow the growth of cells in spheroid formation. After 2-7 days the culture with spheroids are

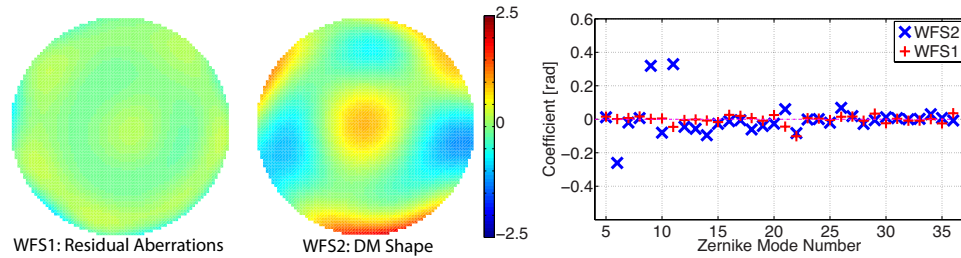


Figure 6. Residual wavefront error by WFS1 (left), a DM shape by WFS2 (middle) for AO on coverslip, and their representation by Zernike polynomials in the Noll's index (right). The residual RMS wavefront error is 0.15 rad while the RMS of the DM shape is 0.57 rad.

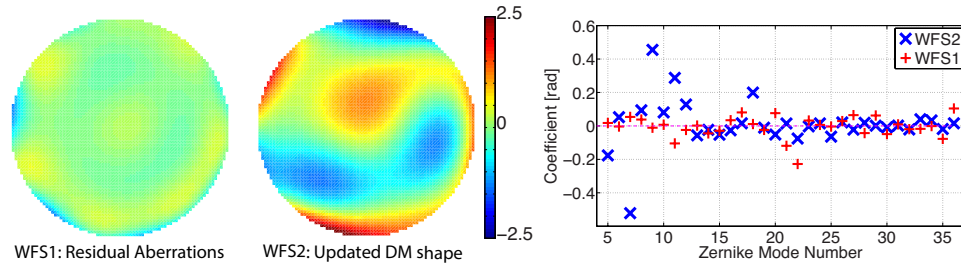


Figure 7. Residual wavefront error after AO compensation by WFS1 (left), the updated DM shape from AO on coverslip by WFS2 (middle), and their representation by Zernike polynomials in the Noll's index (right). The residual RMS wavefront error is 0.36 rad while the RMS of the updated DM shape is 0.83 rad.

centrifuged at 1000 *rpm*, resuspended in 500  $\mu\text{l}$   $\alpha\text{MEM}$  culture medium and were allowed to adhere to a 70% confluent Hep3B cell monolayer on a cover glass for maximally 2 hours. After 1 hour fluorescent beads (FluoSpheres Carboxylate-Modified Microspheres, 0.2  $\mu\text{m}$ , crimson fluorescent (625/645), Life Technologies, Carlsbad, CA, USA) were sprinkled over the cells covering both the Hep3B monolayer as well as the adhered cell spheroids (Fig. 5(a) and Fig. 5(b)). The samples were fixed with 4 % paraformaldehyde for 1-2 hours, washed with Dulbecco's Phosphate Buffered Saline, embedded in Vectashield and mounted to a microscope slide with a custom made plastic spacer ( $\sim 0.75$  mm).

### 3.5 Image Processing for Evaluation

To evaluate the improvement by the AO system quantitatively, FWHM and proposed pinhole intensity ratio are used for recorded fluorescence bead images. For that shot noises should be reduced because both quality measures use maximum intensity, which is easily distorted by them. Therefore, a 3D Gaussian FIR filter with a filter size of  $3 \times 3 \times 3$  pixels and  $\sigma = 0.56$  is applied before calculating the quality measures to smoothen shot noises.<sup>22</sup> After applying the filter to the 3D images, FWHM can be larger and pinhole intensity ratio can be reduced but it does not influence the comparison between no AO case and with an AO compensated case since the reduction by the filter are the same in both cases. With the smoothened images by the filter, the comparison of FWHM and pinhole intensity ratio of multiple beads is more reliable with a small variance and the reduction of outliers.

## 4. EXPERIMENTAL RESULTS

Using the experimental setup in Sec. 3, the developed AO system is evaluated with the calibration method and the evaluation method using an adjustable pinhole. For the evaluation of the calibration method, the aberrations of the optical system are compensated by the beads on the coverslip. After the correction of aberrations induced by the optical system, fluorescence beads at the depth of 40  $\mu\text{m}$  in the cellular spheroid are evaluated. For each case, the pinhole intensity ratio of Eq. (5) is measured for the evaluation of AO correction as well as FWHM.

First the calibration method in Sec. 2.1 is evaluated to compensate for the aberrations of the optical system before introducing specimen. For the calibration (AO on coverslip) 5 airy unit (AU) and 1 AU pinhole are used

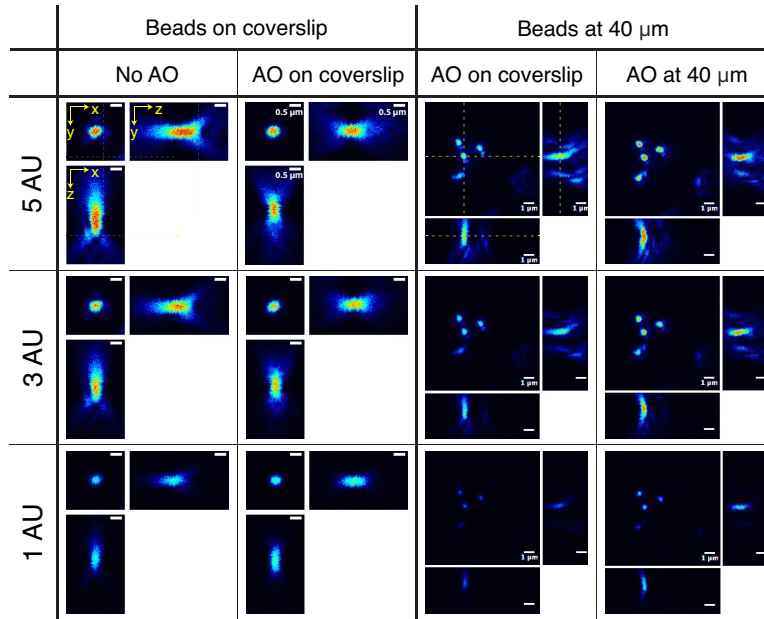


Figure 8. Measured  $xy$ ,  $xz$ , and  $yz$  image slices of  $0.2\mu\text{m}$  fluorescence beads on the coverslip without AO and with AO at coverslip, and the fluorescence beads at a depth of  $40\mu\text{m}$  in the Hep3B cellular spheroid with AO at coverslip and AO at  $40\mu\text{m}$  depth (royal LUT). The measurement is done in three different sizes of the adjustable pinhole of 5, 3, and 1 airy unit (AU). The white scalebar of the images of beads on coverslip represents  $0.5\mu\text{m}$ .

as a big pinhole  $\bar{\gamma}_b$  and a small pinhole  $\bar{\gamma}_s$ , corresponding to  $556.1\mu\text{m}$  and  $111.2\mu\text{m}$ , respectively. For the uncompensated case (No AO), DM is flattened by WFS2 based on the reference path (See dotted black line in Fig. 4). Due to the photobleaching effect of the beads, two different locations are selected for no AO case and AO compensated case, which contains 18 and 13 beads in the scanned area. After an AO correction, 3D images of the beads are recorded with an order of 5 AU, 3 AU and 1 AU and are analyzed for FWHM and the pinhole intensity ratio. Fig 6 shows the residual wavefront error and the final mirror shape of after the calibration process (AO on coverslip) and their representations in Zernike modes. The dominant aberrations shown in the DM shape are astigmatism (6th order), trefoil (9th order) and spherical (11th order) aberrations.

The second experiment is the verification of the designed AO for the correction of specimen-induced aberrations. Three fluorescence beads in the cellular spheroid are chosen for the AO correction, which are at a depth of  $40\mu\text{m}$  from the coverslip. The shape DM is initially set by the aberration compensated case of the first experiment (AO on coverslip), which compensates for the aberrations of the optical system but does not compensate for aberrations induced by specimen. For the correction of the specimen-induced aberration (AO at  $40\mu\text{m}$ ), the DM adapts its shape to reduce the measured aberrations by WFS1 compared to the calibrated reference in the first experiment. In this case, the same location is used before and after the AO correction since a different location can result in different aberrations. To compensate for the intensity degradation by photobleaching, the detector gain is increased for the images with AO at  $40\mu\text{m}$ , which also does not allows a direct comparison of the intensity as the first experiment. Fig 7 shows the residual wavefront error and the updated mirror shape solely by the specimen-induced aberrations from AO on coverslip to AO at  $40\mu\text{m}$ , and their representations in Zernike modes. The dominant aberrations shown in the updated DM shape by AO corrections are coma (7th), trefoil (9th, 18th order), and spherical (11th order) aberrations.

Fig. 8 shows recorded  $xy$ ,  $xz$  and  $yz$  image slices of the fluorescence beads on the coverslip without and with AO correction (left) and the fluorescence beads at  $40\mu\text{m}$  in the cellular spheroid with AO on coverslip and AO at  $40\mu\text{m}$  (right). Aforementioned, the absolute intensity does not show the improvement of the image quality since the beads in the images are not identical or are recorded with different detector gains. Instead, the size and shape of the bead images can be used for the evaluation of the performance enhancement. For the shape with a 5AU pinhole, the uncalibrated bead image shows asymmetric and skewed in  $z$  axis while the image is symmetry

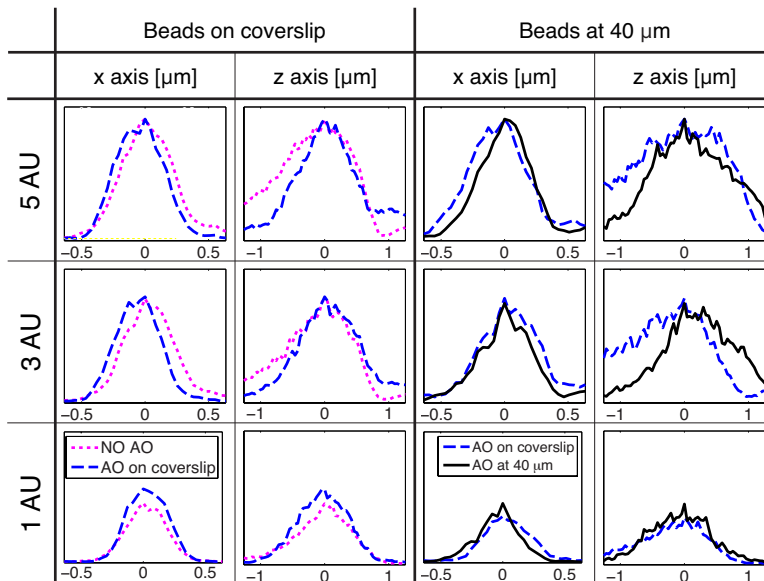


Figure 9. Normalized intensity profiles along  $x$  axis and  $z$  axis of the images in Fig. 8. For the profiles of the beads on coverslip, the intensity is normalized by a scaling factor for matching the maximum intensity with the 5 AU pinhole of each No AO and AO on coverslip case. Then the scale factor of each case is applied to the intensity profiles with 3 AU and 1 AU pinhole to describe relative decrement of intensity. The intensity profiles of the beads at 40  $\mu\text{m}$  processed the same manner.

after AO compensation in  $z$  axis while the images of both No AO and AO on coverslip are similar with a 1 AU pinhole. This is also observed by the axial FWHM with calibration (AO on coverslip), which shows in average 24.9 % improvement than the uncompensated case (No AO) with a 5 AU pinhole, while the improvement in FWHM is not observed with a pinhole of 1 AU. For the correction of specimen-induced aberration, the shape of the image also shows the improvement with less distinct ghosting pattern with AO at 40  $\mu\text{m}$  than with AO on coverslip. The lateral and axial FWHM is also improved with a 5 AU pinhole by 33.7 %, from 1.94  $\mu\text{m}$  to 1.28  $\mu\text{m}$ , while the improvement of FWHM is not observed with a 1 AU pinhole.

While the absolute intensity cannot confirm the image improvement, the proposed pinhole intensity ratio also shows the improvement by the developed AO. To clearly describe the pinhole intensity ratio, Fig. 9 shows normalized intensity profiles by the maximum intensity with 5 AU of the pinhole for each case and experiment. For the beads on coverslip, the maximum normalized intensity with 1 AU pinhole shows that the AO on coverslip case has 29.8 % higher in average than the no AO case. For the beads at 40  $\mu\text{m}$ , the maximum normalized intensity with 1 AU pinhole of the AO at 40  $\mu\text{m}$  case has 18.4 % higher in average than the AO on coverslip case. This shows that the developed AO system with the adjustable pinhole can improve the imaging quality by correcting the aberrations due to the specimen and optical systems, and the improvement can be measured by the proposed pinhole intensity ratio.

## 5. CONCLUSION

This paper presents an adaptive optics development with an adjustable pinhole for a commercial confocal laser scanning microscope. Using the adjustable pinhole, a calibration method and an image quality measure are also proposed to compensate for the aberrations in the optical system and to evaluate the improvement of the image quality by the AO correction, respectively. Fluorescence beads on the coverslip and at a depth of 40  $\mu\text{m}$  in the human hepatocellular carcinoma cell spheroid are used for the experiment. Experimental results verify that the developed AO system can compensate for aberrations of the specimen and can improve the image quality, which is more significant with a big pinhole. The correction of the proposed calibration method using the adjustable pinhole proves its concept with a smaller full width half maximum and the proposed pinhole intensity ratio also indicates this improvement by less intensity degradation with AO compensated images.

For the further research, the selection of the pinhole for the calibration method can be analyzed for a better calibration quality. Since the pinhole intensity ratio has a mismatch with the theoretical value, which needs more investigation. The pinhole intensity ratio also needs to be studied with an extended object for an AO development for CLSM.

## ACKNOWLEDGMENTS

The authors would like to thank Tanjef Szellas, Andrea Pfeiffer, Henk den Hartog from Leica Microsystems for providing the confocal microscope and technical support. This research has been supported by the Integrated Smart Microscopy project in the Smart Optics Systems program of Technologiestichting STW, the Netherlands.

## REFERENCES

1. J. B. Pawley, ed., *Handbook of biological confocal microscopy*, Springer Science Business Media, 3rd ed., 2006.
2. T. Wilson and A. R. Carlini, "Three-dimensional imaging in confocal imaging systems with finite sized detectors," *Journal of microscopy* **149**, pp. 51–66, Aug. 1988.
3. J. Mertz, *Introduction to Optical Microscopy*, Roberts and company publisher, 1st ed., 2009.
4. J. Engelhardt, H. Gugel, and H. Ulrich, "Optical arrangement provided for a spectral fanning out of a light beam," us patent 6801359, 10 2004.
5. M. A. R. Jewel, V. Akondi, and B. Vohnsen, "On pinhole size optimization in wavefront sensorless adaptive optics," in *Adaptive Optics: Methods, Analysis and Applications*, p. OTu1A.3, OSA, (Washington, D.C.), 2013.
6. J. W. Cha, J. Ballesta, and P. T. C. So, "Shack-Hartmann wavefront-sensor-based adaptive optics system for multiphoton microscopy," *Journal of Biomedical Optics* **15**(4), p. 046022, 2010.
7. P. Vermeulen, E. Muro, T. Pons, V. Lorientte, and A. Fragola, "Adaptive optics for fluorescence wide-field microscopy using spectrally independent guide star and markers," *Journal of Biomedical Optics* **16**(7), p. 076019, 2011.
8. X. Tao, J. Crest, S. Kotadia, O. Azucena, D. C. Chen, W. Sullivan, and J. Kubby, "Live imaging using adaptive optics with fluorescent protein guide-stars," *Optics Express* **20**(14), pp. 15969–15982, 2012.
9. X. Tao, Z. Dean, C. Chien, O. Azucena, D. Bodington, and J. Kubby, "Shack-Hartmann wavefront sensing using interferometric focusing of light onto guide-stars," *Optics Express* **21**(25), p. 31282, 2013.
10. S. A. Rahman and M. J. Booth, "Adaptive optics for high-resolution microscopy: wave front sensing using back scattered light," in *MEMS Adaptive Optics VI*, Nov. 2012.
11. S. A. Rahman and M. J. Booth, "Direct wavefront sensing in adaptive optical microscopy using backscattered light," *Applied Optics* **52**(22), p. 5523, 2013.
12. M. Shaw, K. O'Holleran, and C. Paterson, "Investigation of the confocal wavefront sensor and its application to biological microscopy," *Optics Express* **21**(16), pp. 19353–19362, 2013.
13. C. Bourgenot, C. D. Saunter, G. D. Love, and J. M. Girkin, "Comparison of closed loop and sensorless adaptive optics in widefield optical microscopy," *Journal of the European Optical Society: Rapid Publications* **8**(0), p. 13027, 2013.
14. A. J. Wright, D. Burns, B. A. Patterson, S. P. Poland, G. J. Valentine, and J. M. Girkin, "Exploration of the optimisation algorithms used in the implementation of adaptive optics in confocal and multiphoton microscopy," *Microscopy Research and Technique* **67**(1), pp. 36–44, 2005.
15. J. W. Goodman, *Introduction to fourier optics*, Roberts & Company Publishers, 3rd ed., 2005.
16. H. Song, R. Fraanje, G. Schitter, G. Vdovin, and M. Verhaegen, "Controller Design for a High-Sampling-Rate Closed-Loop Adaptive Optics System with Piezo-Driven Deformable Mirror," *European Journal of Control* **17**, pp. 290–301, Jan. 2011.
17. G.-m. Dai, "Modified Hartmann-Shack Wavefront Sensing and Iterative Wavefront Reconstruction," *SPIE Vol. 2201 Adaptive Optics in Astronomy (1994)*, pp. 1–12, Jan. 1994.

18. G. Vdovin, O. Soloviev, M. Loktev, S. Savenko, and L. Dziechciarzyk, "Optimal correction and feedforward control of low-order aberrations with piezoelectric and membrane deformable mirrors," in *SPIE Optical Engineering + Applications*, pp. 81650W–81650W–10, SPIE, Sept. 2011.
19. F. Roddier, *Adaptive optics in astronomy*, Cambridge University Press, 1999.
20. M. Rueckel, J. A. Mack-Bucher, and W. Denk, "Adaptive wavefront correction in two-photon microscopy using coherence-gated wavefront sensing," *Proceedings of the National Academy of Sciences* **103**, pp. 17137–17142, Nov. 2006.
21. J. Zeng, P. Mahou, M.-C. Schanne-Klein, E. Beaurepaire, and D. Débarre, "3D resolved mapping of optical aberrations in thick tissues," *Biomedical Optics Express* **3**(8), p. 1898, 2012.
22. Q. Wu, F. Merchant, and K. Castleman, *Microscope Image Processing*, Academic Press, 2008.